Identification of damage-induced frequency decay on a large-scale model bridge



*Published Version:*
Identification of damage-induced frequency decay on a large-scale model bridge / Tarozzi M.; Pignagnoli G.; Benedetti A.. - In: ENGINEERING STRUCTURES. - ISSN 0141-0296. - ELETTRONICO. - 221:(2020), pp. 111039.1-111039.12. [10.1016/j.engstruct.2020.111039]

This version is available at: https://hdl.handle.net/11585/806544 since: 2021-02-25

*Published:*

DOI: http://doi.org/10.1016/j.engstruct.2020.111039



(Article begins on next page)

# Investigation of damage-induced frequency decay on a large scale model bridge

Mirco Tarozzi [a]*, Giacomo Pignagnoli [a], Andrea Benedetti [a]

*a) Department of Civil, Chemical, Environmental and Materials Engineering, University of Bologna, Viale Risorgimento 2, 40136 Bologna, Italy.*

* Corresponding author.

Phone: +39 051 2093235

Email: mirco.tarozzi4@unibo.it

**Abstract** – Planning the maintenance activity of a civil structure with a life cycle cost-effectiveness requires the evaluation of its functionality in service to identify possible damage states which need a retrofit, avoiding thus danger for the users. In this paper, this topic is explored by using an experimental 1:4 scale model bridge, in which some damage states on the main steel beams are introduced arbitrarily with the aim of detecting the effect of local cracks on the performance of the structure. By performing dynamic tests on the model bridge, it was possible to link the variability of the natural frequencies with the gradual stiffness reduction caused by the cracks. By processing the acceleration signals due to a random excitation of the 6.0x3.0 $m^2$ deck, the main natural frequencies of the bridge have been extracted in several progressive damage states. The observed behaviour was explained by making use of a detailed Finite Elements numerical model. The frequency decay predicted by these methods is in close agreement with the experimental observations and permits to build a useful link between frequency data and damage detection.

*Keywords: Damage detection, Dynamic test, Frequency shift, Operational Modal Analysis, Composite Bridge, Cracked Beam.*

# 1 Introduction

The prediction of the evolving strength and the structural integrity of strategic structures, such as hospitals, rescue buildings or bridges, has attracted the interest of many researchers. Their performance can be shattered by environmental and accidental actions and therefore in the order of avoiding the suspension of the service state, early detection of the damaged condition is mandatory.

Since the last few years of the 20th Century, several non-destructive tests became available to assess the mechanical properties of the materials [1, 2]. Concerning masonry and timber, the authors have recently examined a procedure to characterize them or their health condition [3, 4]. The use of non-destructive methods to estimate the actual health condition of bridges and other civil structures is still in progress and subject of many studies [5, 6]

Unfortunately, often the elements to be tested are not easily attainable, and the material properties can vary inside the structure and among subsequent investigations, causing thus uncertainty in damage estimation. In any case, those methods cannot be used as a continuous process able to show the evolution of the health state of the structure.

In the last years, the collection and the processing of the ambient vibrations became one of the main experimental methods for a global condition assessment of structures through the identification of their dynamic behaviour.

The Operation Modal Analysis (OMA) algorithms have been developed both in the frequency domain and in the time domain to identify main natural frequencies, damping ratios, and mode shapes [7, 8, 9]. The outcomes of different identification techniques, for instance, the Frequency Domain Decomposition (FDD) method [10, 11, 12] and the Stochastic Subspace Identification (SSI) method [13, 14, 15] yield consistent cross-correlated information for the optimization of the finite element (FE) models.

Usually, global modal parameters are functions of the physical properties of the structure. Thus, changes in the physical properties of the structure induce variation in the modal parameters. The topic is still the subject of continuous research [16, 17, 18, 19] aiming at the characterization of the damages in terms of position and intensity. Many tests were carried out almost twenty years ago on full-scale structures and created a solid baseline for the research in the fields of vibration-based Structural Health Monitoring (SHM) and Damage Detection (DD) [20, 21, 22, 23, 24]. The data collected performing those tests are often used as benchmark developing new algorithms or comparing the detection capability and the robustness of different damage indicators [25]. Other methods for detecting damage are currently in progress, taking advantage either of modal strains measured by optical fibres [26] or of recent advances in the information technology, mainly involving artificial neural networks and machine learning approaches [27, 28].

Most of the cited activities used decommissioned bridges in which localized damage scenarios were produced by cutting concrete or steel parts. Lauzon et Al. [29] presented an investigation similar to the one shown here but acting progressively only on one beam. Zhou & Biegalski [30] studied a real damaged bridge with a damage scenario very similar to the one used in the model bridge, but no dynamic investigation was performed. Hagani et Al. [31] listed several damage patches detected in real bridges but any link with the change of dynamic properties was set out. Chajes et Al [32] detailed the damage detected in the I-95 Delaware bridge and the restoration works, but information concerning the bridge stiffness variation is missing.

However, the cited experiments allowed only episodic data collection not linked with the loading level experienced by the bridge. A laboratory scaled model can be loaded and dynamically investigated repeatedly at different load levels, ages, corrosion extent, etc., building so representative correlations of the parameters describing the state, and allowing for future further checks of the extracted data.

Therefore the present study aims to evaluate how local damages, increasing in their severity, influence the natural frequency of a bridge. This is done by assessing the loss of stiffness from frequency decays but neglecting the influence of the damage position.

In particular, the studied experimental model permitted not only to gather a wide set of data in several bridge damage configurations but through the comparison with a 3D FE model did establish a link between the dynamic properties and the damage features which will be useful in planning the condition assessment through dynamic monitoring of real deteriorated full-scale bridges.

Usually, The cost of the monitoring networks installed on most of the highways and civil structures is strongly influenced by the physical characteristic, the level of quality in terms of sensor' technology and number involved in each network.

Concerning the total cost of this kind of networks, the use of a huge number of high-sensitive sensors, their installation and the management of the recorded data may prove to be too expensive for the Public Administration that asks for the service, especially for networks designed for permanent monitoring.

The solution to this problem is to use a proper number of low-cost sensors evenly distributed on the structure or, in other cases, the use of high-sensitive sensors placed at key locations. Limiting the number of sensors is the solution considered in this paper, owing to reduce the network costs and the amount of recorded data as much as possible.

# 2 EXPERIMENTAL TEST

## 2.1 Description of the tested bridge model

The composite steel-concrete bridge deck under study is the 1:4 scaled model of an existing bridge crossing the A14 highway in Italy, near the city of Bologna (Figure 1). The scaling phase involved only the geometrical dimension, whereas the properties of the materials were selected according to the common design practice.

Figure 1. The bridge crossing the A14 highway (on the left) and the scaled model under investigation (on the right).

The model was designed as a tool for checking the ability of dynamic tests in detecting localized damage states. The evaluation was carried out by means of a comparative 3D FE model featuring all the details of the experimental bridge. The performance of the model was calibrated by using a static 4 Point Bending Test (4PBT) as a reference. Then, the prepared FE model was used as a simulation tool in predicting the effect of different damage scenarios.

The construction details and the geometrical data of the model bridge are described in the following. The strength classes and mechanical properties of the materials employed in the construction are summarized in Table 1.

The concrete was obtained with 350 kg/m$^3$ of Portland cement CEM II/A-LL 42.5R, a water-cement ratio varying from 0.53 to 0.59, sand in the range 0.1-1 mm and gravel in the range 5-15 mm complying to a granulometric curve for thin sections. In agreement with the European Standard EN 206 [33], the poured concrete achieved the strength class C28/35 with a density $\rho$ equal to 2300 kg/m$^3$. The cubic compressive strength $R_{ck}$ determined by laboratory tests held 38 MPa. The density was derived by weighing cubic samples. Then, ultrasonic tests were performed on the same specimens to obtain an experimental value of the dynamic elastic modulus. The concrete Young's modulus was finally computed from the dynamic modulus with a mean value roughly equal to 25000 MPa.

Table 1. Mechanical properties of the construction materials employed in the erection of the bridge and applied to the FE model of the bridge.

| Material | Strength Class | Thickness [mm] | Elastic Modulus [MPa] | Density [kg/m$^3$] |
|---|---|---|---|---|
| Structural Steel[1] | S 275 | Various | 210000 | 7860 |
| Concrete[2] | C 28/35 | 130 | 25000 | 2400* |
| Steel Rebar | B 450 C | Ø 8 | 210000 | 7860 |
| Corrugated Steel[1] | S 275 | 0.8 | 210000 | 7860 |
| Neoprene Sheet | Shore A | 15 | 2.5 | 1270 |
| Asphalt | - | 25 | - | 800 |

[1] European Standard EN 10025 and EN 10219 [34, 35]

[2] European Standard EN 206 and UNI-EN 11104 [33]

* The density includes roughly 100 kg/m$^3$ of steel reinforcement.

The bridge is composed of two concrete abutments and a composite deck. Two concrete walls raise from a piled raft foundation made of concrete. The foundations are constrained by six Tubfix piles with a diameter of 127 mm and a length of 6000 mm. The two piers are 3000 mm wide, 1500 mm high and 400 mm thick; such dimensions allow neglecting the piers' contribution to the bridge deck dynamic behaviour.

The deck concrete slab is 6000 mm long and 3000 mm wide. A 55 mm tall stay-in-place zinc-coated structural corrugated steel sheet formwork was adopted to contain the concrete pouring, leading to an average total slab thickness of 130 mm. The slab reinforcement was set out with a bidirectional ø6/100 mm steel mesh and ø8 transversal steel bars placed every 200 mm inside the ribs of the corrugated steel sheet. After the bridge completion, the concrete slab was finished with 25 mm of asphalt (Figure 2, Figure 3).

The steel braced framework illustrated in Figure 4 is fully made of steel S275 and includes three IPE 300 girders, two secondary cross girders made by coupling two UNP 140 and six L 35x4 equal leg angles as cross bracings. Two IPE 300 girders were used as head beams resting over the deck bearings laying on the piers according to the longitudinal section of the bridge showed in Figure 2. The steel framework and the concrete deck are connected by rows of Nelson's shear studs welded every 100 mm over the beam upper flanges.

The bridge deck is sustained by six 15 mm neoprene bearings, posed under the head beams centred to the axis line of the main beams.

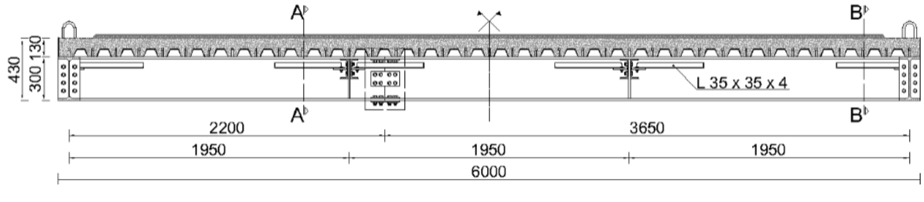


Figure 2. Longitudinal vertical section C-C of the steel deck.

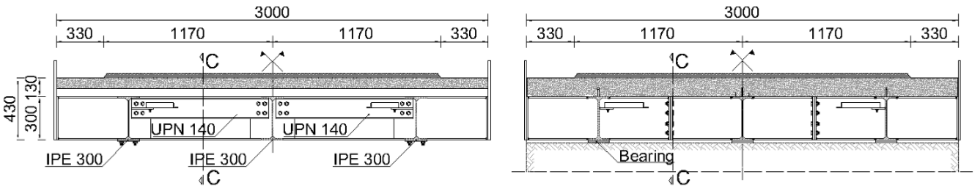


Figure 3. Transverse vertical sections A-A and B-B of the steel deck.

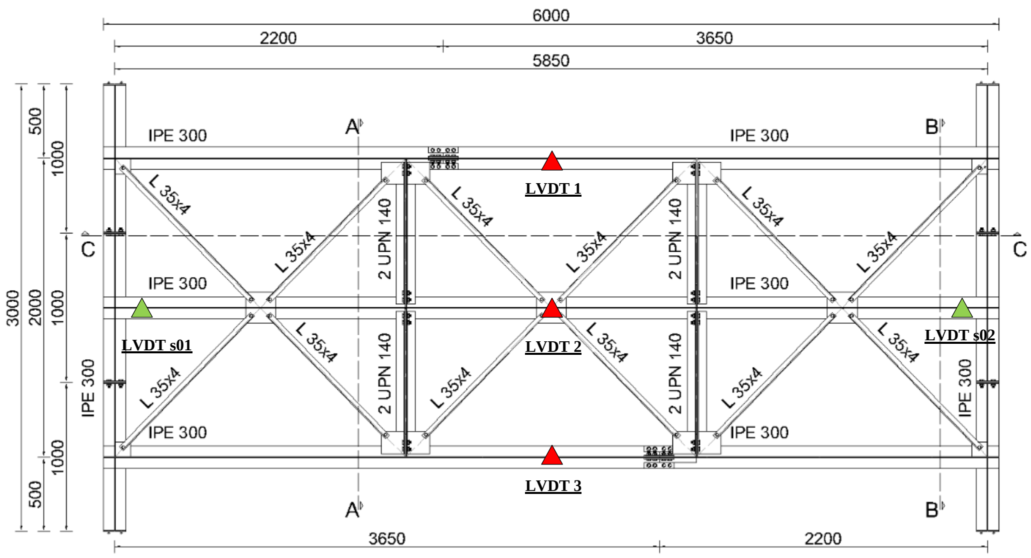


Figure 4. Plan view of the steel grillage and the position of the LVDTs adopted for the static load test (measurement range: red marks 0-50 mm, green marks 0-20 mm).

During the construction phase and the deck casting operation, the structure was not propped. For this reason, the concrete slab shows a non-uniform thickness over its surface due to the uneven deflection of the steel elements. As a concern, the tapered thickness of the slab is causing a frequency shift and switch due to the changed mass distribution, requiring thus very precise modelling if the fit with the experiments is the goal.

As usual, the connection among the main girders and the two head beams was executed with welded joints, while bolted connections linked the secondary cross girders and the bracings together to the main beams. Besides, two more bolted twin plate splices illustrated in Figure 4 and Figure 5 were properly designed for the outer main girders for both the web and the lower flange. These joints were introduced to obtain full continuity, flange break or beam break in one or two beams of the bridge steel framework, encompassing finally five different simulated damage states.

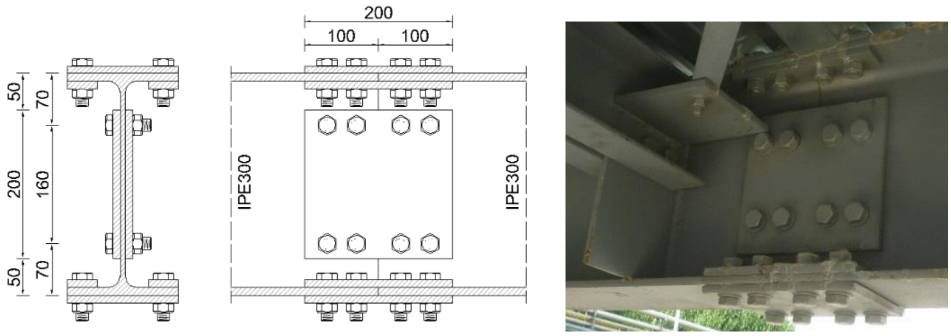


Figure 5: Bolted twin plate splices at one-third of the main beam length.

Naming "D0" the undamaged fully fastened condition, all the following steps consisted in removing a bolted joint of a beam: "D1" means removing the lower flange link on one beam; "D2" refers to the condition in which both flange and web links were removed from the same beam; finally, "D3" and "D4" consisted in replicating the same operations of D1 and D2 on the other outer beam.

## 2.2 Experimental Setup for Static Test

The setup designed for the static test is shown in Figure 6 and Figure 7. The loading beam is composed of two IPE 500 profiles linked by pairs of UPN 300 elements. Two jacks with a capacity of 667 kN act on the beam' ends using Dywidag rods with a diameter of 36 mm running inside the slots of the UPN 300 pairs. The reaction points are set with two pairs of Tubfix piles with diameter Ø 127 mm and length L = 10000 mm designed to balance the maximum forces applied by the two hydraulic jacks. The beam was properly designed by a stiffness criterion, to minimize its deformation during loading.

Figure 6: Static load test setup: on the left is shown the static loading system; on the right is visible the data acquisition system.

Since in the bridge deck there are three main beams and the loading is performed by a pair of beams, there are on the deck six loading points (Figure 7).

The maximum load applied on the bridge didn’t lead to the yielding of the steel members. Thus, the behaviour of the small bridge during the loading phase can be considered fully linear elastic. The linear elastic behaviour allowed to estimate the force exerted by each loading point simply by solving the static scheme of the problem. By considering the huge stiffness of the loading beam, the force acting at each concrete block can be computed following the equilibrium equations governing the whole loading system. Because of the skewness of the loading setup, the forces exerted on the loading points were different. In particular, for each load step, the forces computed at each pair of concrete cubes resulted in the 21%, 33% and 46% of the total applied load *P* for the beams instrumented with the Linear Variable Differential Transducers (LVDT’s) 1, 2 and 3 respectively.

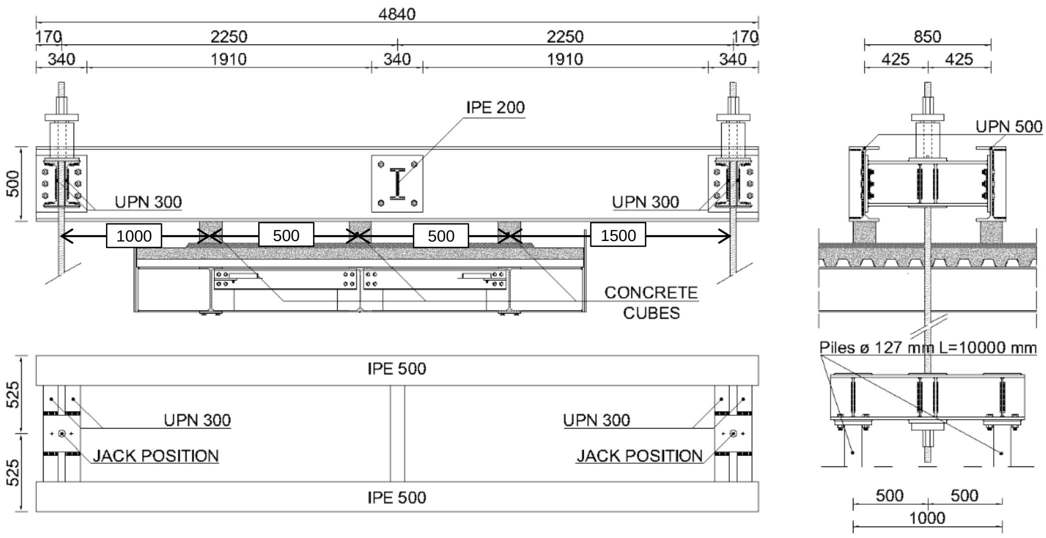


Figure 7: Drawings of the setup of the loading system.

During the experimental campaign, a total of 5 LDTV's recorded the displacements at the five marked positions of Figure 4, while a digital manometer measured the oil pressure provided to the two hollow jacks illustrated in Figure 6 and Figure 7. While three LVDTs (1 to 3) with a measuring range of 50 mm were placed below the mid-span of the main beams, the last two were placed near the supports measuring the deflection of the elastic bearings. The two LVDTs "s01" and "s02" were selected with a range of 20 mm to improve the accuracy of the measure.

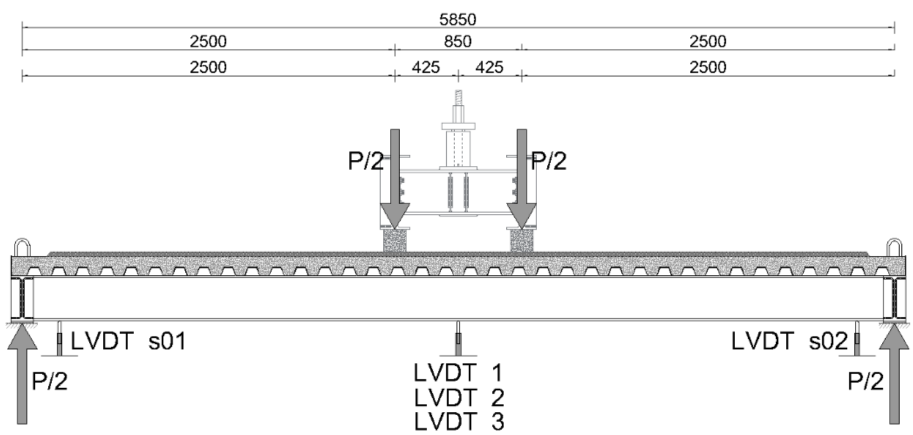


Figure 8: Setup for the static test.

## 2.3 Experimental Setup for Dynamic Test

The main frequencies, damping ratios, and modal shapes were extracted by testing the bridge dynamically taking advantage of the ambient vibrations (AV), a random people walk (RW) and hammer hit (HH) excitations.

Accelerations were measured at a sampling rate of 2000 Hz with a set of eight tri-axial Sensr CX-1 mems accelerometers arranged according to the setup of Figure 9. The CX-1 is an accelerometer developed by SENSR using the MEMS technology, and it can measure the acceleration with the resolution of $10^{-6}$ g within the range ± 1.5g. This sensor was widely used by the authors [36, 37, 38] for other experimental campaigns, and performed very well in all environmental conditions.

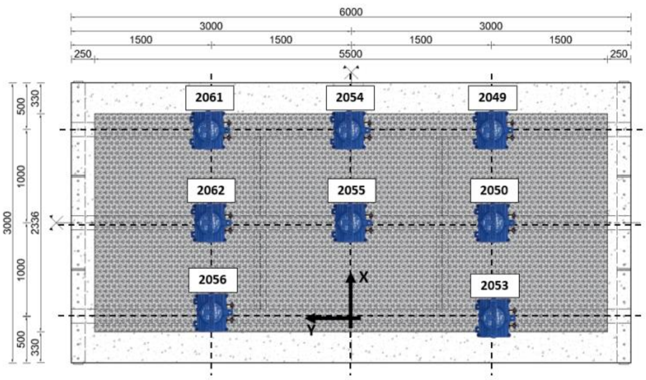


Figure 9: Setup used for the dynamic test.

Although composite steel-concrete decks are orthotropic plates, it is common practice for the dynamic investigation to align many sensors on the axis line of the bridge, while few of them are placed on transversal rows, owing to the detection of torsional modes. In this experimental model, a grid-shape arrangement of the sensors was chosen (Figure 9). Even if by using a greater number of sensors or taking advantage of a multi-setup technique [39, 40] the spatial resolution of the mode shapes and their representation could be improved, the selected minimal setup was able to detect and clearly distinguish the first six mode shapes of interest.

According to the capacity of the recording system, eight CX-1 [41] were used during the initial dynamic identification stage, whereas in the following phases only two accelerometers were employed, considering this setup as typical of continuous damage monitoring in simple bridges. In particular, only the CX-1 named 2056 and 2049 were adopted for the dynamic investigation at each stage of damage realization. These sensors were fixed on the lower flange of the two external beams at a quarter of their length (Figure 10).

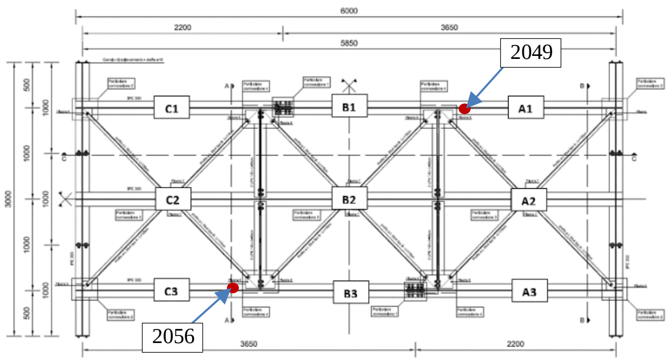


Figure 10. Accelerometers configuration in case of damage stages

All the measurements were performed repeatedly to improve the reliability of the extracted modal parameters. All the tests were completed in a few days with the same daily schedule, aiming to reduce the effect of the environmental conditions. The temperature, roughly equal to 30°C, was the same for all the tests.

## 2.4 Experimental Test Procedure

Once the early version of the FE model was created by following the technical drawings and assigning to the elements the nominal values of specific weight and Young's modulus given by the Italian Standards [42], the experimental tests followed three main steps. Firstly, the dynamic tests were performed to characterize the bridge at its undamaged condition by extracting modal frequencies, modal shapes, and damping ratios; secondly, the static tests allowed estimating the actual static stiffness of both the deck and the rubber bearings. Finally, repeated dynamic tests were carried out after each step of damage from D1 to D4.

According to the setup showed in the previous section, AV and RW excitations were recorded for 30 minutes and 8 minutes respectively, to ensure an acquisition window of at least 2000 times the fundamental period of the bridge. Then, one rubber hammer was used to perform HH excitation in different positions, triggering in this way a large number of the main dynamic modes. Finally, the time series were processed either considering the total length of the signal or processing the acceleration produced by each hammer hit singularly. Since this paper is devoted to investigating the influence of damage on the bending stiffness of the bridge and no significant difference was observed among the frequencies extracted from all the used excitation methods, only the lower main frequencies were extracted and their experimental values were defined by the average of all the completed tests.

The static loading consisted of three sets of ten load cycles starting from 0 kN up to 45 kN, 90 kN, and 140 kN respectively. The bridge was not damaged during the load cycles and its behaviour remained elastic throughout the tests.

# 3 The Finite Element Model

This section illustrates the numerical model of the bridge and the criteria followed to set out proper values of the boundary condition at the supports. The model was solved with the Italian version of the commercial FE software STRAND.

All the mechanical properties of the employed materials are collected in Table 1. Concerning the concrete, the properties were firstly estimated by performing non-destructive tests (NDT) and then inserted into the numerical model. By combining the reference properties given by the Italian Standards [42] and the outcomes provided by NDT data, the starting FE model of the bridge was created.

The sketch of the numerical model is provided in Figure 11, in which each different colour means different mechanical properties assigned to the element.

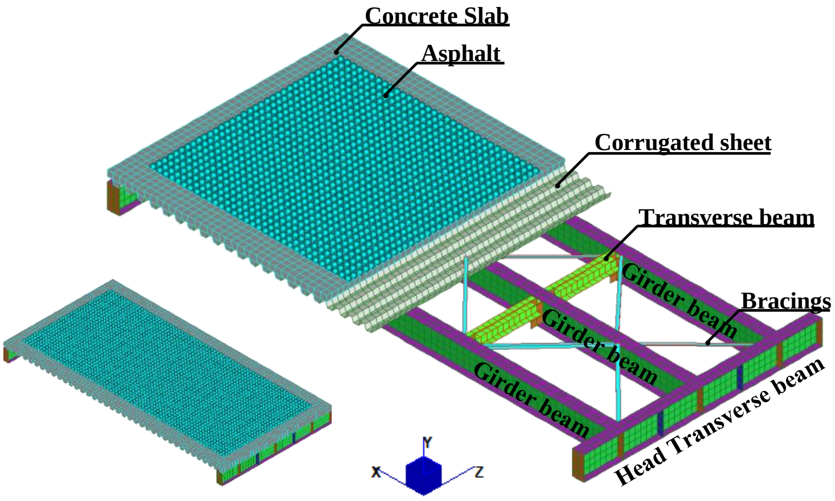


Figure 11: FE numerical model of the steel deck.

Three-dimensional solid 8-node brick elements were used to model the geometry of the concrete slab, while bi-dimensional 4-node shell elements were used to shape the geometry of the main beams, the corrugated steel sheet, and all the steel stiffening plates. Since secondary crossing beams and bracings are bolted to the main steel girders, these parts were introduced as beam and truss elements respectively. The layer of asphalt laying above the concrete slab was defined as a distributed surface mass.

According to what is mentioned in section 2.1, two vertical cuts were provided at a fixed length of the two outer beams of the bridge model, able to simulate the presence of damage. From the mechanical point of view, the two cuts strongly reduced both the stiffness and the load-carrying capacity of the bridge, thus the two bolted twin plate splices illustrated in Figure 5 were properly designed to fully restore the original bending and shear capacity of the solid beams.

However, during the bridge modelling phase, since the stiffness of the bridge was completely restored by the splices and the mass of the plates used for this purpose is negligible compared to the whole mass of the bridge, the two splices were not included in the FE model considering the outer beams as solid beams.

Concerning the load applied during the linear static analyses, the forces computed for each load step were spread as equivalent pressures in 150x150 $mm^2$ square areas on the concrete slab of the FE model. The pressures were set according to the positions of the concrete cubes used for enforcing loads on the bridge beams and the load fractions defined in section 2.2.

The rubber bearings were modelled by using equivalent elastic springs. The standards dealing with bridge bearing devices [43] and the neoprene rubber datasheet [44] allowed a straight calculation of the axial stiffness value of those springs, taking into consideration the incompressibility of the rubber. By assuming the shear modulus $G$ and the shape factor $S$ of the neoprene sheets respectively equal to 0.9 MPa and 2.5, the axial stiffness of the springs was initially set to $7.2 \cdot 10^4$ kN/m.

The calibration of this parameter has played a crucial role during the model updating procedure. In particular, the final value was obtained by matching the experimental Load-Displacement curve measured at the support positions with the results of the Linear Static analyses (LSA) carried out on the FE model. The optimization procedure provided an updated value for the axial stiffness of the springs equal to $6.5 \cdot 10^4$ kN/m, which was then used in the subsequent numerical calculations of both static and dynamic analyses.

It is well known that the elastic modulus of the materials including concrete and rubber, is varying according to the frequency range in which the material is investigated [45, 46]. In particular, the dynamic modulus is usually greater than the static one.

However, in the case study presented here, the structure is mainly composed of steel elements, which do not change their modulus with the excitation frequency. Furthermore, the investigated frequencies are in the range from 0 to 100 Hz, a low-frequency interval in which the difference between static and dynamic modulus can be neglected both for rubber and concrete, although the damping is varying in a meaningful way. It is to remember that ultrasonic testing is in general worked out with probes ranging from 10 to 60 kHz.

# 4 Static and dynamic investigation outcomes of the bridge model

The static tests allowed detecting vertical displacements near the rubber bearings of the central beam, and at the mid-span of the main steel girders. In this way, both the average stiffness of the support and the deck has been derived.

Figure 12 and Figure 13 show a very good agreement among the experimental displacements and those obtained by a series of linear analyses performed by gradually increasing the load applied to the model. In particular, Figure 12 illustrates the values of the two support deflections "*Exp_*" during the loading test compared with those obtained through the numerical LSA. The calibration was set by matching the black line (experimental average), with the results of the central girder supports in the FE model (red line). On the other hand, the static tests allowed also triggering the value of the static Young's modulus for the concrete slab. The tuning of the support stiffness and the concrete elastic modulus led to a very good fit among the experimental and the numerical displacements on the mid-span section for all the three girders (Figure 13).

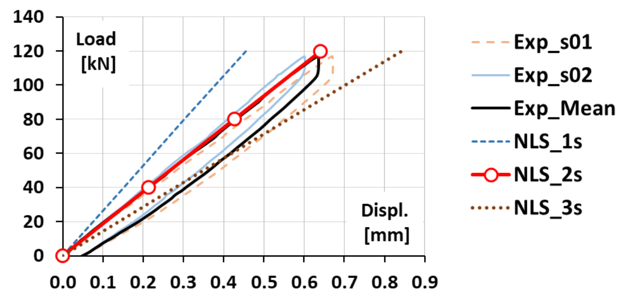


Figure 12. Plot of the Load-Displacement curve measured at the supports compared with the curves of the linear static analysis performed on FE model.

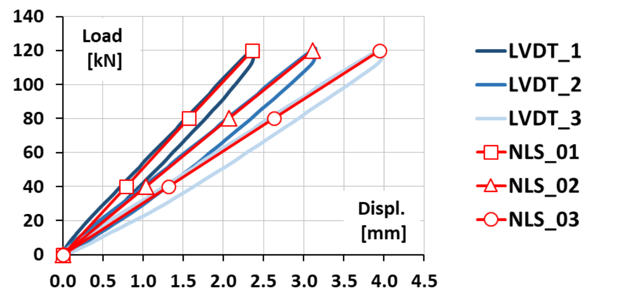


Figure 13. Plot of the Load-Displacement curve measured at the midspan of the main beams and those reconstructed by performing a linear static analysis.

Once the elastic properties of neoprene rubber were calibrated, the values of the mass density of both concrete and asphalt were adjusted by minimizing the distance from the experimental frequencies.

The recorded data were processed using both the frequency and the time domains. The Frequency Domain Decomposition (FDD) [11, 47] and the Stochastic Subspace Identification (SSI-COV) [48, 49, 50], both available in a MatLab Environment [51, 52], were applied to the recorded data.

As previously pointed out, the modal identification was performed by considering the accelerations induced by environmental micro-tremors, hammer hits and people walk. A linear detrending and a resampling up to 500 Hz were applied to the recorded time series and two different output-only identification algorithms were employed to obtain an estimate of natural frequencies and mode shapes.

The vibration modes of the bridge are represented by the local maxima of the first singular value (SV) line (Figure 14), obtained by processing time windows of 16384 samples, considering an overlap of 50% between segments and adopting a Hanning window to reduce the leakage. Then, the SSI_COV algorithm was used to validate the FDD outcomes. The inputs for the SSI method strongly influence their results, for this reason, they were chosen accordingly to what suggested by *Magalhlaes et Al.* [49, 53]. In the present application, good results were achieved with a time lag of 1 second and a model order equal to 140.

The lowest six amplification peaks are sharply shown in Figure 14, in which the first averaged normalized singular value, stable poles and the coherence are identified with the black line, the aligned red circles and the grey line.

A coherence value higher than 0.8 means that the measured signals are well correlated and thus noise shows a low influence. Instead, low coherence values indicate that the signals are strongly influenced by noise. For this reason, the spectrum part associated with coherence lower than 0.8 can be neglected.

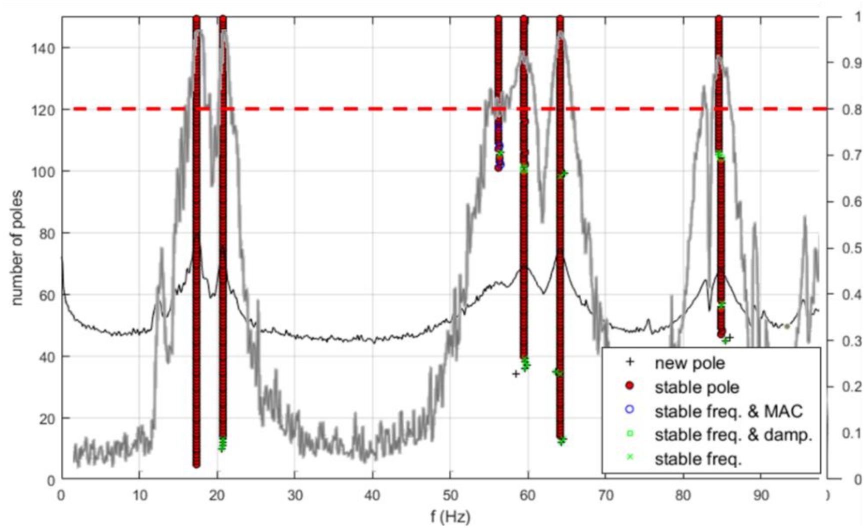


Figure 14: Plot of the first normalized singular value (black line), the SSI plot and the Coherence (grey line).

Table 2 collects the comparison among the extracted experimental frequencies and those obtained carrying out the modal analysis on the FE model. The frequency values listed in Table 2 show a good agreement among numerical and experimental values and a small Coefficient of Variation (CV).

Table 2. List of identified modal shapes, modal frequencies and damping ratio.

| Mode | Mode Type | FDD [Hz] | CV | SSI [Hz] | CV | Dampi ng [%] | Numeri cal [Hz] | Error [-] |
|---|---|---|---|---|---|---|---|---|
| 1 | Bending | 17.6 | 0.40% | 17.6 | 0.21% | 1.9% | 17.6 | 0.0 % |
| 2 | Torsional | 20.8 | 0.00% | 20.8 | 0.08% | 1.4% | 20.4 | 1.9 % |
| 3 | Bending | 59.4 | - | 59.5 | 0.23% | 2.1% | 51.1 | 13.9 % |
| 4 | Torsional | 55.9 | 0.57% | 56.8 | 0.11% | 4.4% | 51.2 | 8.41 % |
| 5 | Plate-like | 64.2 | 0.11% | 64.7 | 0.11% | 0.9% | 66.4 | -3.43 % |
| 6 | Plate-like | 85.0 | 0.17% | 85.3 | 0.18% | 1.4% | 92.8 | 9.18 % |

The deviations between the numerical and the experimental frequency sets are lower than 10% for all but one of the modes and fit almost exactly for the first two modes that were assumed as reference parameters for the damage detection. Even the identified mode shapes (Figure 15), show a good agreement in comparison with those obtained from the FE model Modal Analysis (Figure 16). However, the 3rd mode and the 4th one appear inverted in their positions in Table 2 and Figure 16.

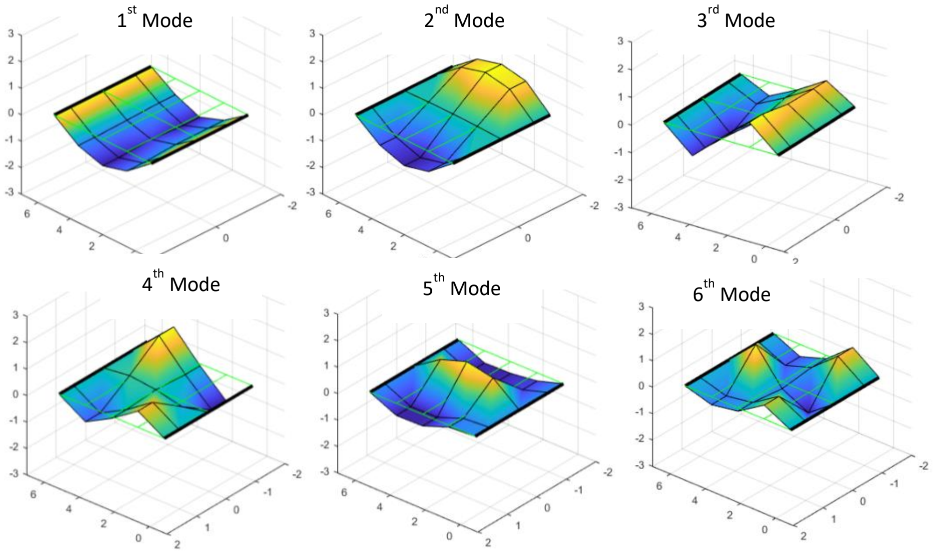


Figure 15. Lowest six mode shapes identified through the operational modal analysis.

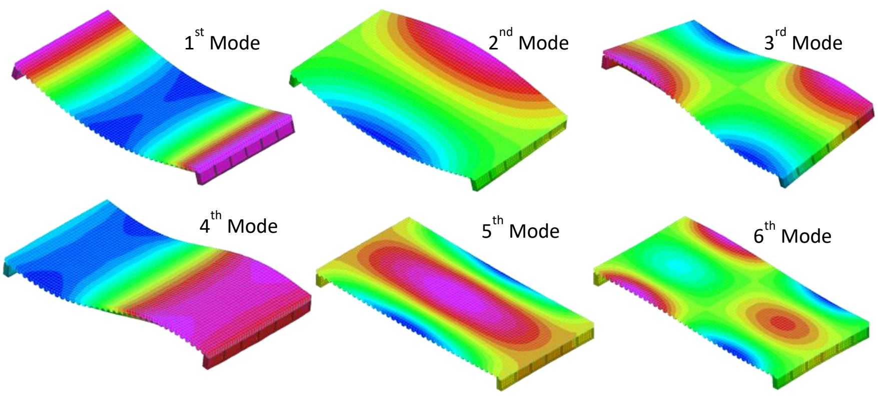


Figure 16. Lowest six mode shapes of the FE model.

The mode correspondence between the experiment and its numerical counterpart can be validated through the so-called Modal Assurance Criterion (MAC):

$$MAC(\varphi_i, \varphi_j) = \frac{\left|\varphi_i^T, \varphi_j\right|^2}{\left(\varphi_i^T \varphi_i\right)\left(\varphi_j^T \varphi_j\right)} \tag{1}$$

By computing the MAC values of the identified mode shapes, the orthogonality error of the modes can be checked (Figure 17). On the other hand, the MAC cross-correlation of the numerical modal shapes with the experimental ones gives a mark of the soundness of the FE model as a counterpart of the real structure.

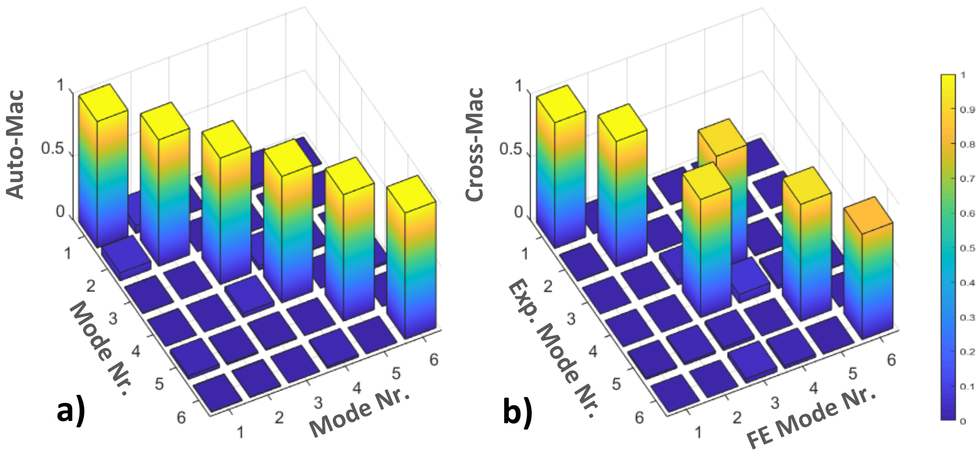


Figure 17. Bar-plots of the AutoMAC (a) and CrossMAC (b) computed on the set of the experimental modal shapes and among the experimental and numerical modal shape sets.

The numerical values of the CrossMAC bar chart depicted in Figure 17.b are listed in the matrix of Table 3.

Table 3. Cross Mac values according to figure 17.b.

| **Mode** | | **Calculated Modes** | | | | | |
|---|---|---|---|---|---|---|---|
| | | **1** | **2** | **3** | **4** | **5** | **6** |
| **Experimental Modes** | **1** | 1.00 | 0.00 | 0.00 | 0.00 | 0.00 | 0.00 |
| | **2** | 0.00 | 0.99 | 0.00 | 0.00 | 0.00 | 0.00 |
| | **3** | 0.00 | 0.00 | 0.04 | 0.91 | 0.01 | 0.01 |
| | **4** | 0.00 | 0.00 | 0.94 | 0.07 | 0.03 | 0.01 |
| | **5** | 0.01 | 0.02 | 0.02 | 0.00 | 0.93 | 0.00 |
| | **6** | 0.00 | 0.00 | 0.04 | 0.02 | 0.00 | 0.84 |

# 5 Effects of the presence of local damages

The damage equivalent to a crack involving the flange, or the flange and the web of a beam, was obtained by removing respectively the flange bolted twin splice plates, or both the flange and the web splice plates (Figure 18).

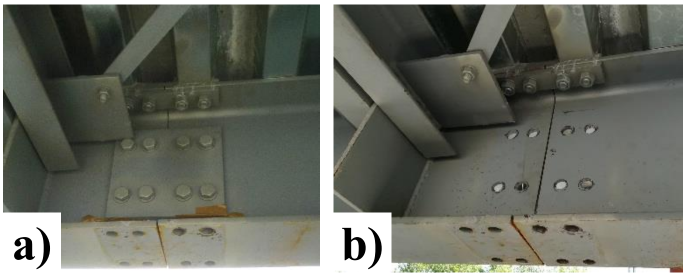


Figure 18. Progressive removal of the bolted plates: (a) removal of the bottom flange splice plates, (b) removal of flange and web splice plates.

Since the simulated damage in the beams consists of a vertical cut in the unbolted sections,  this geometry change was obtained in the FE model by deleting a row of elements in the selected positions. In particular, the removal of the bolted splice plates in the bottom flange of the left side beam represents the damage phase D1; the removal of both the flange and the web splice plates of the same beam denotes the damage phase D2. By adding to this state the removal of the splice plates of the lower flange in the right side beam, the phase D3 is attained; progressing with the last web splice plates removal the maximum damage phase D4 is obtained.

The presence of the simulated damage in the numerical model was taken into account by cutting away the shell elements filling the gap between the two disconnected (unbolted) flange or web plates. For the sake of illustration, the damage conditions D1 and D2 are sketched in the following figure (Figure 19), by representing the portion around the cut section.

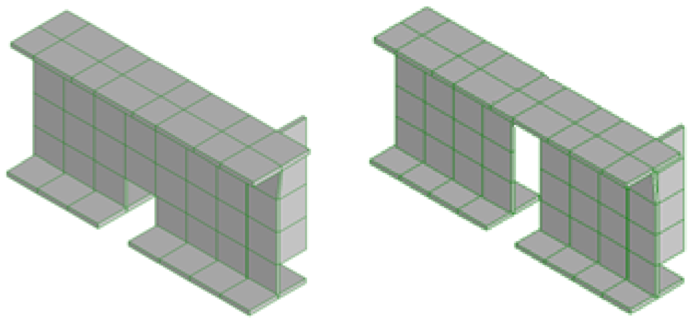

Figure 19: On the left the damaged condition D1, while, on the right, the Condition D2.

At the end of the experimental campaign, all the data of the subsequent four damage phases were processed, by extracting the variations of the two lowest frequencies. Then, the variations of the same frequencies were computed from the model by progressively deleting the elements simulating the damages as in figure 12. In this way, the data reported in Figure 20 were obtained.

Both the first and the second mode are very sensitive to the damage. The experimental data showed an almost linear reduction in frequency with the progressive severity of the damage state.

The FE simulation led to a very good fit between the detected frequencies with those obtained performing the numerical modal analysis on the progressively changed model. The relative error on all the phases remained always below 3% of the experimental value. The dynamic tests were performed using only two accelerometers without a roving sensor technique [54]. It allowed to sharply identify only the first two natural frequencies, the decay of which is illustrated in Figure 20 describing all the damage states. Since the aim of the paper concerns the evaluation of the stiffness and the fundamental frequency variations due to the damage level, higher modes were not taken into account. Further analyses will allow observing variation related to higher frequencies and mode shapes too. In particular, the analysis of higher mode shapes needs significant improvements in the spatial resolution of the sensors.

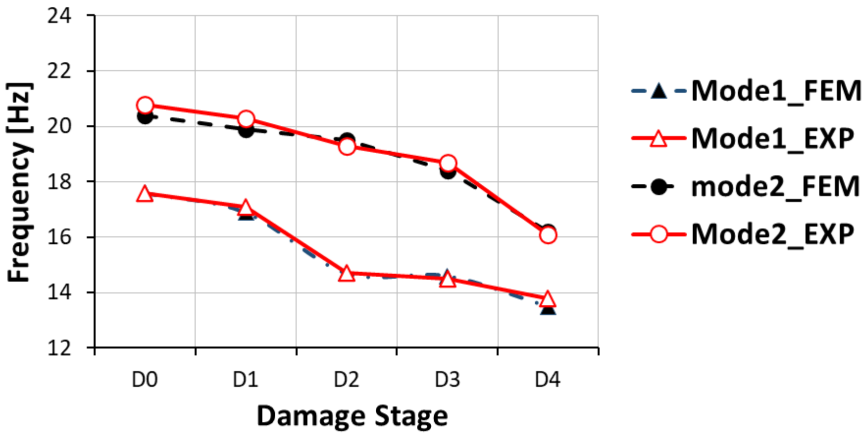


Figure 20. Frequency decay due to the presence of damage

Table 4. Comparison between numerical, experimental and analytical frequencies for each damage phase.

| Freq. | D0 [Hz] | D1 [Hz] | D2 [Hz] | D3 [Hz] | D4 [Hz] |
|---|---|---|---|---|---|
| $F_{1,exp}$ | 17.6 | 17.1 | 14.7 | 14.5 | 13.8 |
| $F_{1,mod}$ | 17.6 | 16.9 | 14.7 | 14.6 | 13.5 |
| $F_{1,an}$ | 17.6 | 16.4 | 15.7 | 13.1 | 12.0 |
| | | | | | |
| $F_{2,exp}$ | 20.8 | 20.3 | 19.3 | 18.7 | 16.1 |
| $F_{2,mod}$ | 20.4 | 19.9 | 19.5 | 18.4 | 16.2 |
| $F_{2,an}$ | - | - | - | - | - |

Table 4 lists detected and obtained frequencies in the four increasing damage states. Once the distributed mass, the bending stiffness and the torsional constant were computed according to the mechanical properties of the materials and the geometry of the bridge, analytical formulas for the frequencies were used in validating the FE model. The results obtained by solving the closed-form formulas governing the dynamic equilibrium of an equivalent beam [55, 56] are very similar to the values obtained from the numerical model.

Starting from values of bending rigidity $EJ$ and torsional rigidity $Gk_t$ equal to $1.35 \cdot 10^5\ kNm^2$ and $4.27 \cdot 10^4\ kNm$, respectively, and keeping constant values of distributed mass $\rho A$ and rotational inertia $\rho J_p$ respectively equal to 916 kg/m and 0.804 kNm the analytical values of the lowest bridge natural frequencies can be easily computed. The frequency related to the first mode was computed for all the damage states by introducing the rigidity modification for the elements simulating the damaged zones. Concerning the fundamental frequency, both experimental outcomes and analytical calculations correctly evaluated the reduction in terms of stiffness. In particular, a decrease of 13%, 20%, 33%, and 40 % of total stiffness was estimated through the frequency values extracted from the dynamic tests. The analytical stiffness decay computed for the damage conditions D1, D2, D3, and D4, are respectively 8%, 30%, 31% and 41% with a good match of the experimental values.

# 6 Conclusions

This paper presents detailed data of an experimental campaign carried out on a 1:4 scaled model of a composite steel-concrete bridge deck. In the range up to 100 Hz, eight vibration modes were distinctly identified. A very good agreement was found between the experimental modes and those provided by the FE model except for the third and fourth modes, that are switched between the experiments and the calculations. The MAC computed convolving the two sets of numerical and identified modal shapes showed high cross-correlation values, although a swap between third and fourth mode was detected. This small misfit is probably a consequence of the non-uniform thickness of the concrete deck caused by the self-weight sagging of the deck during the concrete pouring operations.

Local damages simulated in two of the main beams produced important shifts in the values of the first two main frequencies. The observed decay in terms of frequency shows a high sensitivity of the fundamental frequency concerning the presence of progressive damage.

Further analyses are in progress looking at the evolution of modal shapes and damping ratios in connection to several mixed combinations of damage obtained by varying the sequence of bolted cover plates removal. The investigation of the retrofit of the cut beams by using carbon fibre patch repairs of the flange and web discontinuities is planned in a further study on the model bridge.

# 7 Acknowledgements

The construction of the scaled model of the deck was an important task addressed with the financial support from the ERA-NET Infravation 2014 research program through the SHAPE project (Predicting Strength Changes in Bridges from Frequency Data - Safety, Hazard, and Poly-harmonic Evaluation) under Grant 31109806.004. The support of the Infravation program is gratefully acknowledged. COGEI building group contributed to the realization of the bridge discussed in this paper by following the design drawings provided by the authors. The authors thank Roberto Bianchi and Mario Marcolongo for the help of supporting all the tests.

**Compliance with Ethical Standards:** The project SHAPE and the research program Infravation completely comply with the ethical standards required by the European Community for research granting.

**Conflict of Interest:** The authors declare that they have no conflict of interest.

# 8. References

[1] K. L. Rens, T. J. Wipf e F. Klaiber, «Review of nondestructive evaluation techniques of civil infrastructure,» *Journal of Performance of Constructed Facilities,* 1997. DOI: 10.1061/(ASCE)0887-3828(1997)11:4(152)

[2] D. McCann e M. Forde, «Review of NDT methods in the assessment of concrete and masonry structures,» *NDT and E International,* vol. 34, n. 2, pp. 71-84, 2001. DOI: 10.1016/S0963-8695(00)00032-3

[3] A. Benedetti e M. Tarozzi, «Toward a quantitative evaluation of timber strength through on-site tests,» in *Advances in Engineering Materials, Structures and Systems: Innovations, Mechanics and Applications - Proceedings of the 7th International Conference on Structural Engineering, Mechanics and Computation, 2019*, Cape Town, 2019. DOI: 10.1201/9780429426506-300

[4] A. Benedetti e M. Tarozzi, «Interpretation formulas for in situ characterization of mortar strength,» *Construction and Building Materials,* vol. 242, pp. 1-11, 2020. DOI: 10.1016/j.conbuildmat.2020.118093

[5] G. Spencer, L. Hung Manh, L. Tuan, N. Luan, S. Ryan e P. Huy, «Nondestructive evaluation sensor fusion with autonomous robotic system for civil infrastructure inspection,» *Journal of Field Robotics,* pp. 988-1004, 2018. DOI: 10.1002/rob.21791

[6] K. L. Rens, C. Nogueira e D. J. Transue, «Bridge management and nondestructive evaluation,» *Journal of Performance of Constructed Facilities,* vol. 19, pp. 3-16, 2005. DOI: 10.1061/(ASCE)0887-3828(2005)19:1(3)

[7] R. Brincker, «Some Elements of Operational Modal Analysis,» *Shock and Vibration,* pp. 1-11, 2014. DOI: 10.1155/2014/325839

[8] R. Brincker e C. E. Ventura, Introduction to Operational Modal Analysis, Wiley Blackwell, 2015.

[9] S. R. Ibrahim, J. C. Asmussen e R. Brincker, «Modal Parameter Identification from Responses of General Unknown Random Inputs,» in *14th International Modal Analysis Conference*, Dearborn, Michigan, USA, 1996.

[10] N. J. Jacobsen, P. Andersen e R. Brincker, «Applications of Frequency Domain Curve-fitting in the EFDD Technique,» in *Conference Proceedings of the Society for Experimental Mechanics Series, 2008, IMAC-XXVI: Conference and Exposition on Structural Dynamics - Technologies for Civil Structures*, New York, 2008.

[11] R. Brincker, L. Zhang e P. Andersen, «Modal identification of output-only systems using frequency domain decomposition,» *Smart Materials and Structures,* vol. 10, n. 3, pp. 441-445, 2001. DOI: 10.1088/0964-1726/10/3/303

[12] R. Brincker e L. Zhang, «Frequency domain decomposition revisited,» in *IOMAC 2009 - 3rd International Operational Modal Analysis Conference, p 615-626, 2009,* 2009.

[13] B. Peeters e G. De Roeck, «Reference-based stochastic subspace identification for output-only modal analysis,» *Mechanical Systems and Signal Processing,* vol. 13, n. 6, pp. 855-878, 1999. DOI: 10.1006/mssp.1999.1249

[14] B. Peeters e G. De Roeck, «Stochastic System Identification for Operational Modal Analysis: A Review,» *Journal of Dynamic Systems, Measurement, and Control,* vol. 123, n. 4, pp. 659-667, 2001. DOI: 10.1115/1.1410370

[15] P. Kirkegaard e P. Andersen, «State space identification of civil engineering structures from output measurements,» in *Proceedings of the International Modal Analysis Conference - IMAC*, 1997.

[16] G. De Roeck, A. Teughels e E. Reynders, «Damage identification of civil engineering structures based on operational modal data,» in *Proceedings of the 1st International Operational Modal Analysis Conference, IOMAC*, 2005.

[17] S. W. Doebling, C. R. Farrar e M. B. Prime, «Summary review of vibration-based damage identification methods,» *Shock and Vibration Digest*, vol. 30, n. 2, pp. 91-105, 1998. DOI: 10.1177/058310249803000201

[18] F. Magalhães, A. Cunha e E. Caetano, «Vibration based structural health monitoring of an arch bridge: From automated OMA to damage detection,» *Mechanical Systems and Signal Processing*, vol. 28, pp. 212-228, 2012. DOI: 10.1016/j.ymssp.2011.06.011

[19] C. Gentile, M. Guidobaldi e A. Saisi, «One-year dynamic monitoring of a historic tower: damage detection under changing environment,» *Meccanica*, vol. 51, n. 11, pp. 2873-2889, 2016. DOI: 10.1007/s11012-016-0482-3

[20] J. Maeck e G. De Roeck, «Damage assessment using vibration analysis on the Z24-bridge,» *Mechanical Systems and Signal Processing*, vol. 17, n. 1, pp. 133-142, 2003. DOI: 10.1006/mssp.2002.1550

[21] J. Maeck, B. Peeters e G. De Roeck, «Damage identification on the Z24 bridge using vibration monitoring,» *Smart Materials and Structures*, vol. 10, n. 3, pp. 512-517, 2001. DOI: 10.1088/0964-1726/10/3/313

[22] M. Döhler, F. Hille, L. Mevel e W. Rücker, «Structural health monitoring with statistical methods during progressive damage test of S101 Bridge,» *Engineering Structures*, vol. 69, pp. 183-193, 2014. DOI: 10.1016/j.engstruct.2014.03.010

[23] C. Farrar, W. Baker, T. Bell, K. Cone, T. Darling, T. Duffey, A. Eklund e A. Migliori, «Dynamic characterization and damage detection in the I-40 bridge over the Rio Grande,» Los Alamos, 1994. DOI: 10.2172/10158042

[24] C. R. Farrar, P. J. Cornwell, S. W. Doebling e M. B. Prime, «Structural Health Monitoring Studies of the Alamosa Canyon and I-40 Bridges,» Los Alamos, 2000.
DOI: 10.2172/766805

[25] P. F. Giordano e M. P. Limongelli, «Vibration-based damage identification for the S101 benchmark bridge: A comparison of indicators,» in *9th European Workshop on Structural Health Monitoring, EWSHM 2018*, Manchester, UK, 2018.

[26] D. Anastasopoulos, M. De Smedt, L. Vandewalle, G. De Roeck e E. P. Reynders, «Damage identification using modal strains identified from operational fiber-optic Bragg grating data,» *Structural Health Monitoring*, vol. 17, n. 6, pp. 1441-1459, 2018. DOI:

10.1177/1475921717744480

[27] A. Ibrahim, A. Eltawil, Y. Na e S. El-Tawil, «A Machine Learning Approach for Structural Health Monitoring Using Noisy Data Sets,» *IEEE Transactions on Automation Science and Engineering,* pp. 900-908, 2020. DOI: 10.1109/TASE.2019.2950958

[28] S. B. Beheshti Aval, V. Ahmadian, M. Maldar e E. Darvishan, «Damage detection of structures using signal processing and artificial neural networks,» *Advances in Structural Engineering,* vol. 23, n. 5, 2020. DOI: 10.1177/1369433219886079

[29] R. G. Lauzon e J. T. DeWolf, «Ambient Vibration Monitoring of a Highway Bridge Undergoing a Destructive Test,» *Journal of Bridge Engineering,* vol. 11, n. 5, pp. 602-610, 2006. DOI: 10.1061/ ASCE 1084-0702 2006 11:5 602

[30] Y. Zhou e A. Biegalski, «Investigation of large web fractures of welded steel plate girder bridge,» *Journal of Bridge Engineering,* vol. 15, n. 4, pp. 373-383, 2010. DOI: 10.1061/(ASCE)BE.1943-5592.0000111

[31] R. Haghani, M. Al-Emrani e M. Heshmati, «Fatigue-Prone Details in Steel Bridges,» *Buildings,* vol. 2, pp. 456-476, 2012. DOI: 10.3390/buildings2040456

[32] M. Chajes, D. Mertz, S. Quiel, H. Roecker e J. Milius, «Steel Girder Fracture on Delaware's I-95 Bridge over the Brandywine River,» in *Asce Structures Congress 2005*, New York, 2005. DOI: 10.1061/40753(171)36

[33] "EN 206: Concrete - Specification, performance, production and conformity".

[34] «EN 10025: Hot rolled products of structural steel».

[35] «EN 10219: Cold formed welded steel structural hollow sections».

[36] A. Tomor, J. Nichols e A. Benedetti, «Identifying The Condition Of Masonry Arch Bridges Using Cx1 Accelerometer,» in *ARCH 2016*, Wroclaw, Poland, 2016.

[37] A. Benedetti, M. Tarozzi, G. Pignagnoli e C. Martinelli, «Dynamic Investigation and Short-Monitoring of an Historic Multi-span Masonry Arch Bridge,» in *ARCH 2019*, Porto, Portugal, 2020. DOI: 10.1007/978-3-030-29227-0_92

[38] J. Nichols, A. Tomor e A. Benedetti, «Use Of Accelerometer Technology For Quantifying Condition Of Masonry Arch Bridges,» in *13th Canadian Masonry Symposium*, Halifax, CA, 2017.

[39] M. Dohler, E. Reynders, F. Magalhaes, L. Mevel, G. De Roeck e A. Cunha, «Pre- and Post-identification Merging for Multi-Setup OMA with Covariance-Driven SSI,» in *Dynamics of Bridges, Volume 5*, 2011.

[40] E. Reynders, F. Magalhaes, G. De Roeck e A. Cunha, «Merging Strategies for Multi-Setup Operational Modal Analysis: Application to the Luiz I steel Arch Bridge,» in *IMAC-XXVII*, Orlando, Florida USA, 2009.

[41] SENSR, «CX1 Network Accelerometer & Inclinometer,» [Online]. Available: https://sensr.com/downloads/R001-420-V1.0%20CX1%20Network%20Accelerometer%20and%20Inclinometer%20User%20Guid

e.pdf.

[42] I. I. a. T. ministry, Aggiornamento delle «Norme tecniche per le costruzioni», 2018.

[43] «CNR 10018/85 – Apparecchi di appoggio per le costruzioni, Istruzioni per l'impiego».

[44] F. Industriale, «Rubber sheets and mats datasheet».

[45] X. Lu, Q. Sun, W. Feng e J. Tian, «Evaluation of dynamic modulus of elasticity of concrete using impact-echo method,» *Construction and Building Materials,* vol. 47, pp. 231-239, 2013.

[46] B.-J. Lee, s.-h. Kee, T. Oh e Y.-Y. Kim, «Evaluating the Dynamic Elastic Modulus of Concrete Using Shear-Wave Velocity Measurements,» *Advances in Materials Science and Engineering,* vol. 5, pp. 1-13, 2017.

[47] R. Brincker, L. Zhang e P. Andersen, «Modal identification from ambient responses using frequency domain decomposition,» in *Proceedings of the International Modal Analysis Conference - IMAC,* 2000.

[48] F. Magalhães, Á. Cunha e E. Caetano, «Dynamic monitoring of a long span arch bridge,» *Engineering Structures,* vol. 30, n. 11, pp. 3034-3044, 2008.
DOI: 10.1016/j.engstruct.2008.04.020

[49] F. Magalhães, Á. Cunha e E. Caetano, «Online automatic identification of the modal parameters of a long span arch bridge,» *Mechanical Systems and Signal Processing,* vol. 23, n. 2, pp. 316-329, 2009. DOI: 10.1016/j.ymssp.2008.05.003

[50] P. van Overschee e B. De Moor, Subspace identification for linear systems: Theory,, New York, NY: Kluwer Academic Publishers, 1996.

[51] A. Otto, «OoMA Toolbox, MATLAB Central File Exchange,» [Online]. Available: https://www.mathworks.com/matlabcentral/fileexchange/68657-ooma-toolbox.

[52] E. Cheynet, «Operational modal analysis with automated SSI-COV algorithm,» 2020. [Online]. Available: https://www.github.com/ECheynet/SSICOV.

[53] F. Magalhaes e A. Cunha, «Explaining  operational modal analysis with data from an arch bridge,» *MechanicalSystemsandSignalProcessing,* vol. 25, pp. 1431-1450, 2010.

[54] J. Zhang, K. Maes, G. De Roeck, E. Reynders, C. Papadimitriou e G. Lombaert, «Optimal sensor placement for multi-setup modal analysis of structures,» *Journal of Sound and Vibration,* vol. 401, pp. 214-232, 2017. DOI: 10.1016/j.jsv.2017.04.041

[55] M. Rades, Mechanical Vibrations I, Printech, 1990.

[56] S. S. Rao, Mechanical vibrations, Prentice Hall, 2010.